Cellulose acetate membranes treated with titanium dioxide and cerium dioxide nanoparticles and their nanocomposites for enhanced photocatalytic degradation activity of methylene blue

B. Aljawrneh[1], A. Alsaad[2,*] ⓘ, B. Albiss[3], S. Alrousan[2], A. Alshanableh[2], and S. Mutlaq[4]

[1] *Department of Physics, Al-Zaytoonah University of Jordan, P.O. Box 130, Amman 11733, Jordan*

[2] *Department of Physics, Jordan University of Science and Technology, P.O. Box 3030, Irbid 22110, Jordan*

[3] *Nanotechnology Institute, Jordan University of Science and Technology, P.O. Box 3030, Irbid 22110, Jordan*

[4] *Department of Nutrition and Food Technology, Jordan University of Science and Technology, P.O. Box 3030, Irbid 22110, Jordan*

ABSTRACT

We report on the photocatalytic degradation activity of methylene blue (MB) using Cellulose acetate (CA) membranes embedded by metal oxide nanoparticles (NPs). Titanium dioxide and Cerium dioxide (TiO_2 and CeO_2) and their nanocomposites are used as nanofillers in CA membranes to enhance photocatalytic activity. The casted nanocomposite membranes are synthesized using the phase inversion method and characterized using X-ray diffraction, X-ray fluorescence, scanning electron microscopy, Fourier-transform infrared spectroscopy, and UV–Vis to investigate structural, surface morphological, elemental content, and the optical properties. In particular, surface morphological and optical results are analyzed to elucidate a deeper understanding of porosity and photocatalytic activity via the degradation of the MB dye. The as-prepared CA–NP membranes are tested for photocatalytic degradation of MB by exposing the membrane/MB dye combination to UV illumination for different exposure times. Results reveal that CA–TiO_2 membrane exhibits the smallest nanopore size, the most efficient exciton separation, and the largest surface area as compared with CA–CeO_2 and CA–TiO_2–CeO_2-casted membranes. Consequently, CA–TiO_2 membrane shows a good cyclic photocatalytic degradation activity (about 64%). Furthermore, the obtained MB degradation activity follows the increasing trend: CA–TiO_2 membrane (Energy gap E_g = 3.26 eV, Absorption activity $A\% = 64\%$) > CA–TiO_2–CeO_2 membrane (E_g = 3.33 eV, $A\% = 15\%$) > CA–CeO_2 (E_g = 3.4 eV, $A\% = 7\%$) that is directly correlated with the values of the E_g of the NP component of the membranes, the high porosity, and large surface area of the membrane. This suggests the synergetic use of the two metal

Address correspondence to E-mail: alsaad11@just.edu.jo; amalsaad@unomaha.edu
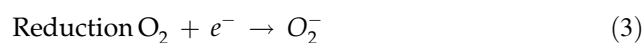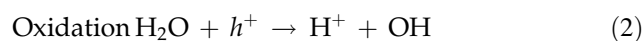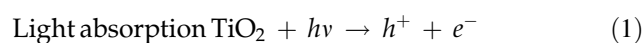
oxides in potential applications of the photocatalytic degradation of MB and other organic pollutants for water treatment.

1 Introduction

The increased world population put a tremendous pressure on water resources, as well as the decrease in surface water reserves and the increase in water demands around the world have urged the need for efficient water treatment and recycling techniques [1]. Cellulose (CA) membrane-based technology has imminent importance for water purification technology and catalytic application owing to their low cost and high permeation. However, self-cleaning and separation of salt charge ions from CA membranes limits its large-scale applications. Therefore, new approaches have suggested treating CA membranes by embedding inorganic metal oxide nanoparticles (NPs) into the CA membranes to enhance their functionalities as water purifying agents. A big challenge facing the world is to secure enough quantities of clean drinkable water to meet the increased global needs [2]. For the last decades, metal oxide NPs have been used to enhance photocatalytic activity of different types of water treatment agents. Inorganic and organic contaminations have caused serious health issues for the vast majority of the world population as drinking water is concerned [3–5]. Recently, the standard wastewater treatment methods implementing nonporous polymeric membranes coated with appropriate catalytic NPs have increasingly been used commercially. The advantage of using such membranes is their efficiency for eliminating both organic and inorganic contaminations [6]. Methylene blue (MB) is well known to be a highly toxic organic compounds that can cause serious water pollution for large number of drinking water resources around the globe [7]. Water treatment implementing photocatalytic activity to degrade pollutants to standard acceptable international levels has been shown to be quite simple and less expensive in comparison with other water treatment techniques. Furthermore, efficient reduction of highly toxic organic pollutants from drinking water can be achieved using different NPs that are known to improve the efficiency of photocatalytic procedures [8]. For instance, metal oxide–semiconductors such as Titanium dioxide (TiO$_2$) is one of the most common photocatalytic materials owing to its low cost, low toxicity, and chemical stability [9, 10]. Additionally, it exhibits an optical band gap energy (E_g) that is appropriate for efficient photocatalytic process [11, 12].

Fujishima et al. [13] experiment sparked the use of photocatalytic techniques for water treatment and splitting. In their original experiment, water splitting of the contaminated water was achieved under UV light using a TiO$_2$ electrode immersed into hydrogen and oxygen with minimal possible consumption of energy. Photocatalytic process depends on the generation of free radicals. Thus, a reaction takes place with unwanted organic components in wastewater, causing a degradation of these components [14, 15], as shown in the following equations:

$$\text{Light absorption } TiO_2 + hv \rightarrow h^+ + e^- \tag{1}$$

$$\text{Oxidation } H_2O + h^+ \rightarrow H^+ + OH \tag{2}$$

$$\text{Reduction } O_2 + e^- \rightarrow O_2^- \tag{3}$$

In general, the oxidation and reduction phases occur simultaneously in standard photocatalytic process as present in the schematic diagram shown in Fig. 1. In general, the reduction/oxidation potential of the adsorbate should be at appropriate level with regard to the energy band level of the metal oxide or nanocomposite to allow the photocatalytic process. According to the normal hydrogen electrode (NHE) scale the conduction band of the metal oxide should be more negative than the reduction potential of H$^+$/H$_2$ and the valence band should be more positive than the oxidation potential of the OH$^-$/H$_2$O to be oxidized [16]. In addition, the photocatalytic process is driven by the equilibrium state between fermi level potential and the chemical potential of adsorbates. Also, the photocatalytic activity is influenced by the oxidation state of the surface and the redox potential of the adsorbates, which strongly affects the charge flow between the surface and adsorbates [17]. When the electronegativity of the adsorbate is much higher than that of the reduced surface, the charge transfer from the surface to the adsorbate is observed [18]. However, the values of E_g ranging between 1.5 and

Fig. 1 A schematic of the general mechanism of photocatalytic degradation
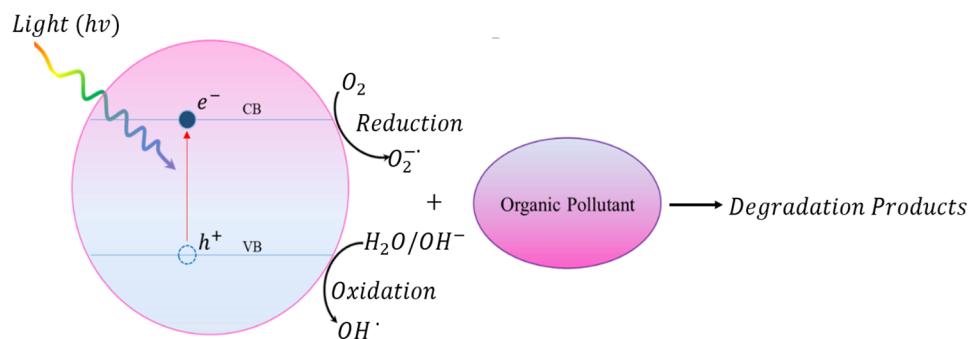
3.5 eV exhibited by certain semiconductors facilitate the simultaneous occurrence of oxidation and reduction stages [13]. Finally, the incident photon energy should exceed the E_g of the metal oxide to ensure efficient charge separation and migration through the active surface sites. The mechanism of photocatalytic degradation using NPs such as TiO_2 - under UV irradiation ($\lambda > 360 \, nm$) can be proposed as follows: the photodegradation of unwanted organic pollutants involves the excitation of the TiO_2 by UV light, generating electron–hole pairs and resulting in photodegradation of organic pollutants present in the wastewater [19].

Lately, NP membranes have attracted great attention for a wide range of nanotechnology applications, such as wastewater treatment and water purification [20]. Organic cellulose membranes incorporated with deposited or embedded NPs have been used for a highly efficient photocatalytic degradation [21], owing to their biodegradability, chemical resistance, and thermal stability, as well as highly reactive surface functional groups [22]. Such nanocomposite membranes can enhance the photocatalytic degradation due to their dual functionality, flexibility, specific chemical reactivity, extraordinary mechanical properties, and strong thermal stability [23]. The TiO_2 NPs have been reported as suitable hydrophilic fillers for enhancing the mechanical characteristics of polymeric membranes. As a result of its strong interaction with polymer structures, integrating TiO_2 into the membrane matrix has a favorable influence on their properties [24]. Furthermore, its excellent compatibility with organic solvents permits the formation of good dispersive nanocomposite membranes that are homogeneous with practically no aggregation [25].

The aims of this work is twofold. Firstly, to verify the influence of TiO_2, CeO_2 NPs, and their nanocomposite on the nanostructures and photocatalytic activity of the fabricated CA membranes.

Secondly, to investigate the effect of the two metal oxide NPs embedded in the CA membrane on the nanoporosity of nanocomposites' CA membrane and thus on the permeation of water. The details of the degradation mechanism are highlighted and are confirmed to be related to the surface area and pore size of the CA–NP membranes. The novelty of this work is based on the advantages of simultaneous incorporation of CeO_2 and TiO_2 into the CA membrane to yield CA–TiO_2–CeO_2 nanocomposite. This incorporation controls the higher recombination rate of electron–hole. Therefore, it acts as electron donor for creating more cation/anion in the nanocomposite matrix. Furthermore, the higher amount of oxygen content in CeO_2 NPs enhances the degradation of MB dye. It shields the valence bands that reduce the recombination and thus enhance the MB degradation. Moreover, synergy between the photocatalytic degradation of MB by the two metal oxides is demonstrated and discussed.

2 Materials and methods

2.1 Reagents and materials

Commercial-grade cellulose acetate (CA), Cerium (IV) oxide (CeO_2) nanopowder < 25 nm, MB, and dimethylformamide (DMF) are purchased from Sigma-Aldrich, Inc., St. Louis, MO, USA. Titanium oxide (TiO_2) nanopowder (40 nm) is purchased from US Research Nanomaterials, Inc., Houston, USA.

2.2 Preparation of TiO_2, CeO_2, and TiO_2–CeO_2 NP membranes

CA–TiO_2 flat sheet membranes were prepared by the phase inversion method [26]. A 5 wt% TiO_2 NPs were dissolved in DMF. The mixture was sonicated for

15 min to disperse the NPs uniformly into the solution. Then CA (wt% = 17.5) was added to the initial mixture for 30-min intervals and left to dissolve in the solvent for 24 h while stirring. The agitation was conducted for 24 h to ensure the optimal dispersion of the NPs in the polymer solution. The same procedure was applied for the CA–CeO$_2$ at wt% = 5% membrane. However, for CA–TiO$_2$–CeO$_2$ nanocomposite membrane, the CeO$_2$ NPs of wt% = 2.5% and TiO$_2$ NPs of wt% = 2.5% are mixed together. Finally, the mixture is added to the DMF solution.

The casting solutions were then kept for 24 h to eliminate air bubbles. Then, casting solutions are deposited on a mirror plate using spin coater "Laurell WS-650-23" [27] at 1500 rpm for 10 s. The casting films are subsequently immersed in a distilled water bath at room temperature to complete the phase separation process [28]. A schematic diagram of the preparation technique of CA–NP membrane is shown in Fig. 2. The irradiation UV light source at 365 nm (UVP C-70G chromate-Vue Cabinet, Ultraviolet Sources: 254 nm UV of 1290 μW/cm^2 and 365 nm UV of 2100 μW/cm^2) used to perform the photocatalytic degradation activity of the three as-prepared CA–NP membranes.

2.3 Characterization techniques

The prepared CA–NP membranes are optically characterized using a UV–Vis spectrophotometer (U-3900H). Structural properties of the CA–NP membranes are measured by Powder X-ray diffraction (XRD) (Malvern Panalytical Ltd, Malvern, UK) (220–230 VAC 50/60 Hz 40 A) using Cu-Kα radiation of 1.542Å in wavelength, where the patterns were recorded using Bragg's configuration 2θ of range 10–70. Morphologies of CA–NP membranes are measured and analyzed using scanning electron microscopy (SEM, Quanta FEG 450). The absorption spectra of the MB degradation were recorded between 190 and 1100 nm of the samples on a spectrophotometer (EMC-16PC-UV). Tracing the concentrations of TiO$_2$ and CeO$_2$ NPs in the CA–TiO$_2$–CeO$_2$ nanocomposite is performed using X-ray Fluorescence technique (NEX QC + QuantEZ, Rigaku).

3 Results and discussion

3.1 Surface morphology of the investigated membranes and their nanocomposites

Membrane morphology of all investigated synthesized loaded membranes is described by measuring the SEM cross-sectional images. The SEM micrographs are used to elucidate the effect of incorporating NPs embedded in the CA membrane. Figure 3 illustrates the SEM profiles of the cross-sectional views of synthesized pure CA and CA–TiO$_2$, CA–CeO$_2$, and CA–TiO$_2$–CeO$_2$ nanocomposite membranes. A closer look at the SEM cross-sectional profiles reveals that most characteristics of the membrane morphologies are significantly affected by

Fig. 2 A schematic illustrates the experimental setup used for preparing CA–NP membranes
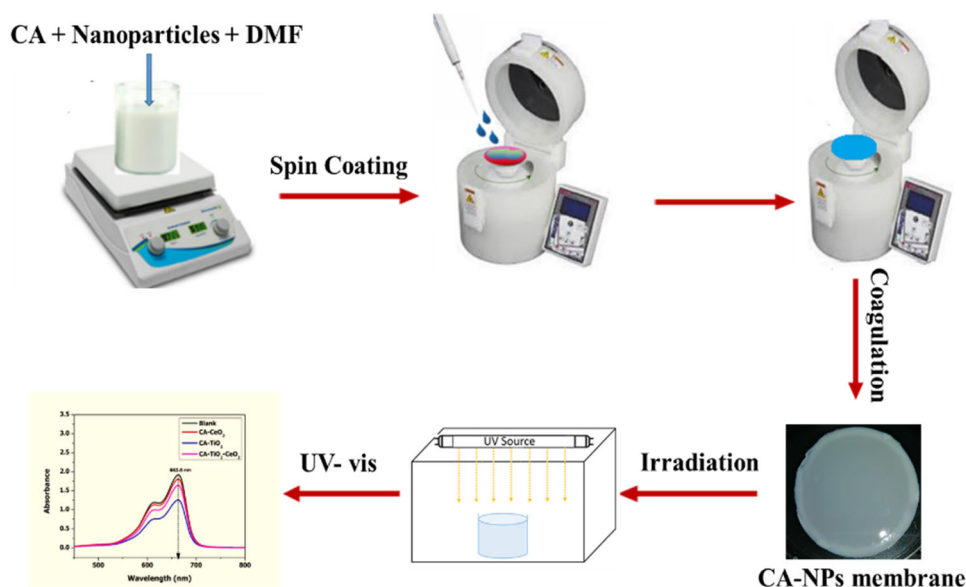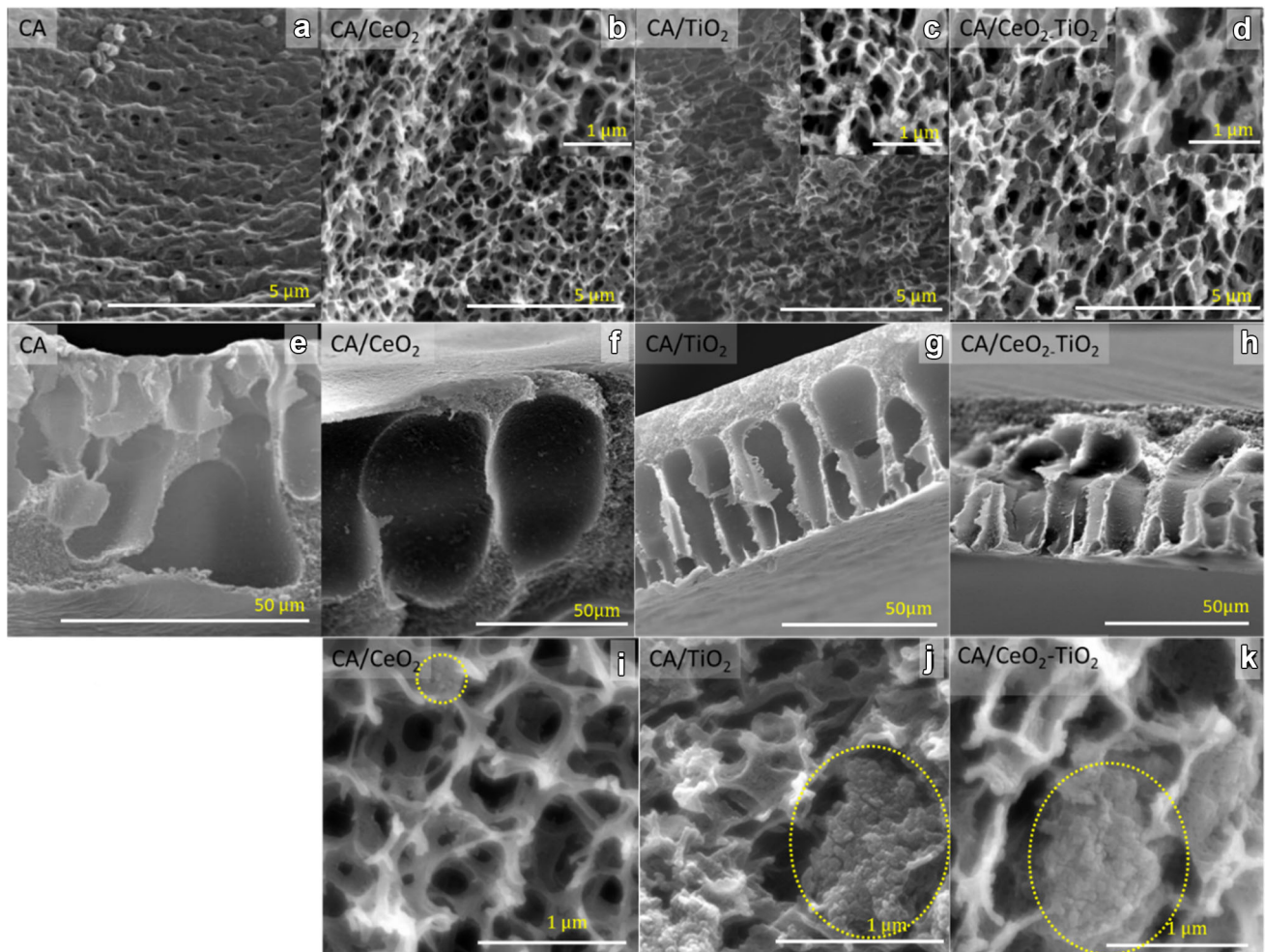
Fig. 3 **a**, **e** The SEM cross-sectional micrographs of the pristine CA membrane, **b**, **f** CA–CeO$_2$ membrane, **c**, **g** CA–TiO$_2$ membrane, and **d**, **h** CA–TiO$_2$–CeO$_2$ membrane, **i**–**k** nanoparticles of CA–CeO$_2$, CA–TiO$_2$, and CA–TiO$_2$–CeO$_2$ embedded inside the membrane, respectively. The circled cross-sections of figures **i**, **j**, and **k** demonstrate clearly the distribution of CeO$_2$, TiO$_2$, and TiO$_2$–CeO$_2$ nanoparticles

the loading of TiO$_2$ and CeO$_2$ NPs as shown in Fig. 3a to d: in particular, the pore size and the order of the sublayer. It can be seen that the NPs dispersed well inside the membranes with an average pore size nearly 200 nm for CA–TiO$_2$, 250 nm for CA–CeO$_2$, and 400 nm for CA–CeO$_2$–TiO$_2$ of the sublayer. A well-oriented sublayers are constructed in the case of CA–TiO$_2$. The loaded CA membranes exhibit high permeability and good hydrophobic properties. Therefore, the loaded membranes are expected to provide high antifouling properties for ions in desalination water. Such interesting properties make the loaded nanocomposite membranes eligible to be potential candidates for effective water treatment and recycling process. It is worth noting that nanopore size of the sublayer is important to water permeation

and nanofiltration process. Consequently, the synthesis process of preparing effective membranes should take into account their abilities to prevent pores blockage of sublayer. A dense and small size pores are observed during the formation of the CA–TiO$_2$ and CA–CeO$_2$ membranes resulting in high porous morphology compared to large size pores and less dense porous sublayer of CA–TiO$_2$–CeO$_2$. This result can be explained in terms of strong interaction between ions of TiO$_2$ and CeO$_2$ NPs in the CA matrix leading to pore blockage and larger size of pores. Figure 3e to h shows the cross sections of the morphologies of all the prepared membrane nanocomposite samples. Closed macro-voids with thick walls are detected in all samples. A thick and dense skin was observed for the deposited membranes. A close

look at the SEM micrographs of the three investigated CA–NP membranes yields the following results:

1. CA–CeO$_2$ has a thickness of 87 μm.
2. CA–TiO$_2$ membrane has a thickness of 56 μm.
3. CA–CeO$_2$–TiO$_2$ membrane has a thickness of 67 μm. In addition, SEM images reveal a well ordered and homogenous macro-void for CA–CeO$_2$ membrane.

3.2 XRD analysis

Crystal structures of the membrane samples are investigated by Powder X-ray Data Analysis System. To elucidate and interpret the major diffraction peaks, XRD patterns of CA, CA–TiO$_2$, CA–CeO$_2$, and CA–TiO$_2$–CeO$_2$ nanocomposite membranes are measured and recorded as shown in Fig. 4. The dispersive broad peak $2\theta \sim (20^o - 30^o)$ demonstrates the amorphous structure of CA. To identify the major peaks associated with different crystallographic planes, we analyze the XRD spectra of each investigated CA–NP membrane. The XRD pattern of CA–TiO$_2$ membrane reveals a high intensity peak at 25.3^o corresponding to Miller indices (101) crystallographic planes [29–31], which is associated with anatase crystalline structure of TiO$_2$. Titanium dioxide (TiO$_2$) may crystallize in three different phases, namely, anatase, rutile, and brookite [32]. Anatase is a tetragonal metastable phase of TiO$_2$ [33] and possesses intense XRD diffraction peak which appears at (101) plane.
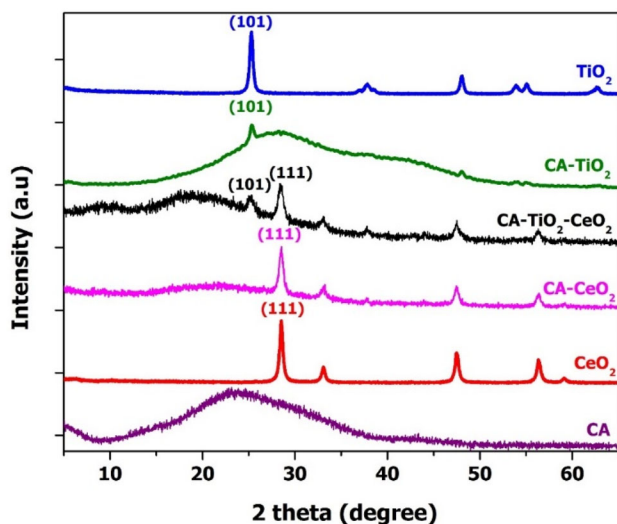

Fig. 4 The XRD patterns of pristine CA, CA–TiO$_2$, CA–CeO$_2$, and CA–TiO$_2$–CeO$_2$ nanocomposite membranes

Figure 4 shows that CA–CeO$_2$ membrane exhibits a major peak at $2\theta = 29^o$ associated with crystallographic planes indexed by (111) Miller indices which is in good agreement with previous experimental findings [34]. Interestingly, the XRD patterns of CA–TiO$_2$–CeO$_2$ nanocomposite membrane identifies two major peaks in the pattern associated with (101) and (111) crystallographic planes matching the corresponding peaks of the individual CA–TiO$_2$ and CA–CeO$_2$ membranes confirming homogeneous embedding of TiO$_2$ and CeO$_2$ NPs into the CA matrix.

3.3 Fourier-transform infrared spectroscopy (FTIR)

Figure 5a shows the Fourier-transform infrared spectroscopy (FTIR) of pristine CA, CA–TiO$_2$, CA–CeO$_2$, and CA–TiO$_2$–CeO$_2$ nanocomposite membranes. The vibrational modes of the CA–NP membranes are investigated in the (400–4000 cm^{-1}) spectral range. The FTIR spectrum reveals that C=O and C–O stretching vibration modes of COOH carboxylic acid group are located at 1732 cm^{-1} and 1032 cm^{-1} for CA–TiO$_2$, CA–CeO$_2$, and CA–TiO$_2$–CeO$_2$ nanocomposite membranes [35]. The weak absorption spectrum located at 1451 cm^{-1} and 900 cm^{-1} is related to the O=C–OR and C–H groups. The stretching vibrational band located at 1217 cm^{-1} is assigned to epoxy C–O bond of the three investigated CA–NP membranes [36]. The broad absorption peaks observed in the FTIR profile of CA–TiO$_2$ and CA–TiO$_2$–CeO$_2$ membranes in the (3000–3500 cm^{-1}) spectral range are associated with the hydroxyl group O–H. This vibrational mode could be assigned to the interaction between the O–H group of cellulose membrane and Ti–O bond in TiO$_2$ nanoparticle [37]. In addition, it reveals a strong interfacial interaction between TiO$_2$ nanoparticle and cellulous membrane. The low absorption band of O–H can be attributed to the weak interaction between O–H group of cellulose and Ce–O bond of CeO$_2$ nanoparticle. The FTIR results are in good agreement with the previously reported findings on photocatalytic activity of CA–NP membranes [38–40]. The X-ray fluorescence spectroscopy (XRF) is a powerful analytical technique that provides both qualitative and quantitative analyses of nanocomposites. The trace of elements in the geometrical nanocomposite membrane is performed using XRF.
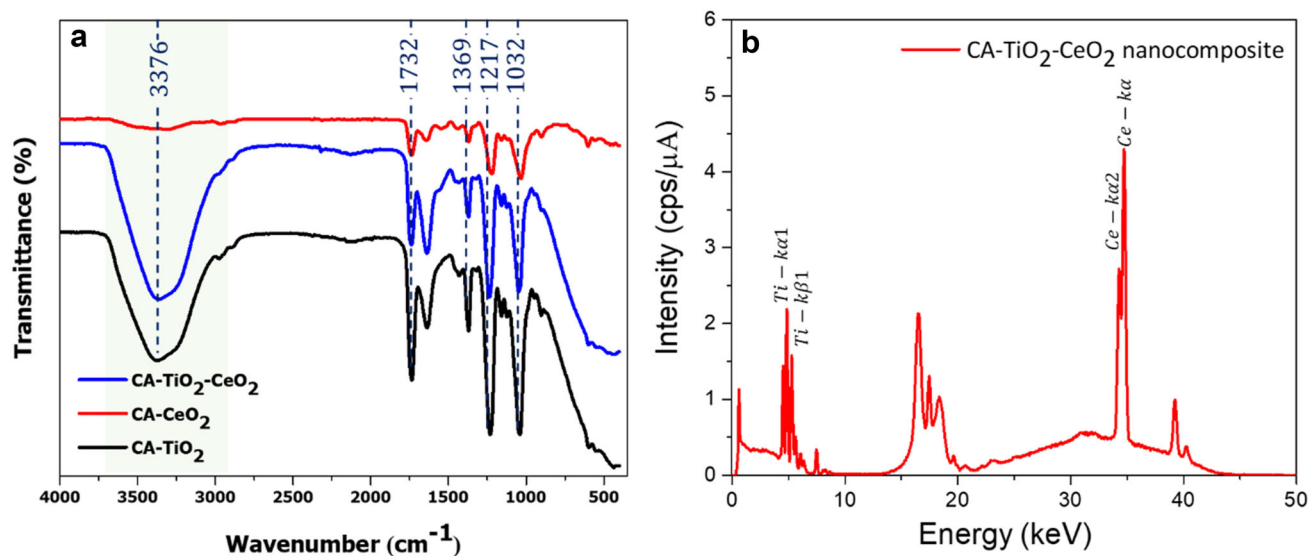
Fig. 5 **a** The Fourier-transform infrared spectroscopy (FTIR) of pristine CA, CA–TiO$_2$, CA–CeO$_2$, and CA–TiO$_2$–CeO$_2$ nanocomposite membranes and **b** the X-ray fluorescence (XRF) of CA–TiO$_2$–CeO$_2$ nanocomposite membranes

Since CA–TiO$_2$–CeO$_2$, nanocomposite membrane contains high abundances of elements for which absorption and fluorescence effects can be reasonably realized using XRF spectroscopy. Elemental analysis of the CA–TiO$_2$–CeO$_2$ nanocomposite membrane is performed by employing EDXRF (NEX QC + QuantEZ, Rigaku) as shown in Fig. 5b. The relatively non-destructive chemical analysis performed in this work yields EDXRF spectra that reveals the presence of 46.6% of TiO$_2$ NPs and 34.6% of CeO$_2$ NPs in CA–TiO$_2$–CeO$_2$ nanocomposite membranes.

3.4 Photocatalytic activity evaluation

The photocatalytic activity of all prepared membranes is tested for MB photocatalytic degradation. By comparing the photocatalytic activity of different CA–NP membranes, we found that CA–TiO$_2$ NP membrane exhibits the optimum degradation activity. Careful inspection of Fig. 6 indicates that CA–TiO$_2$ has a photocatalytic degradation activity of about 64% as compared to that of CA–CeO$_2$ NP (7%) and CA–TiO$_2$–CeO$_2$ NP (15%) membranes. This could be attributed to the values of the optical E_g of the three CA–NP membranes (3.26 eV, 3.33 eV, and 3.4 eV), respectively.

Since TiO$_2$ NPs exhibit the lowest E_g, their ability to facilitate the absorption of UV light to generate exciton that enhances the reduction and oxidation process is stronger than the other two investigated membranes.
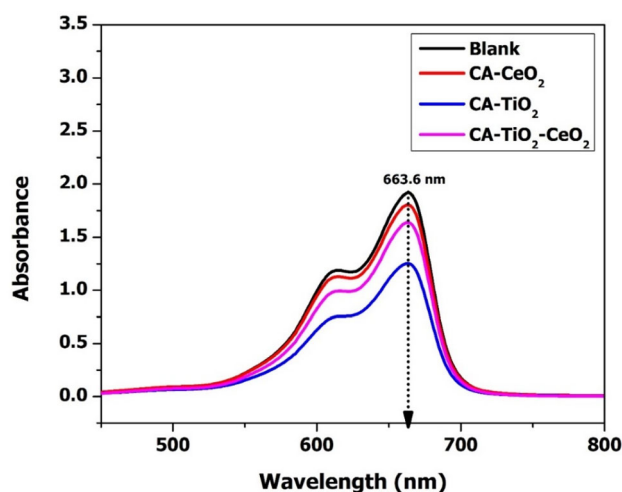

Fig. 6 The photocatalytic degradation of MB by different membranes (CA, CA–TiO$_2$, CA–CeO$_2$, and CA–TiO$_2$–CeO$_2$ nanocomposite) exposed to UV light irradiation

The photocatalytic degradation activity of the three CA–NP membranes is tested by measuring the degradation of (MB). In order to confirm the photocatalytic degradation activity of MB, a pollutant solution is prepared by mixing 1 mg of MB into 100 mL of deionized water. The three types of membranes are individually immersed into the MB-pollutant solution. Each membrane is irradiated with a source of UV light source at 365 nm (UVP C-70G chromate-Vue Cabinet, Ultraviolet Sources: 254 nm UV of 1290 μW/cm^2 and 365 nm UV of 2100 μW/cm^2). For each CA–NP

membrane type, each of the eight different samples (mixture of CA–NPs and MB) are irradiated with a UV light for an exposure period of 15 min sequentially. The total exposure time for the eight samples of each CA–NP and MB is thus 120 min. The absorption spectrum of each sample is investigated using UV–Vis spectrophotometer [41] with a total internal sphere (EMC-16PC-UV). To elucidate the photocatalytic MB degradation activity, the absorbance is measured for the 190–1100 nm spectral range. The residual content of MB in the membrane-MB mixture is measured at $\lambda = 664$ nm (typical for MB), as can be obviously seen from the abrupt clinch of the peak for each membrane–MB mixture in comparison with that of MB itself labeled as Blank. Clearly, the optimum intensity of the absorbance peak for the Blank, CA, CA–TiO$_2$, CA–CeO$_2$, and CA–TiO$_2$–CeO$_2$ nanocomposite membranes is observed at practically the same wavelength ($\lambda = 664$ nm). Upon illumination with the UV light, the intensity of the absorbance is significantly reduced.

To obtain a deeper insight into the high degradation activity of CA–TiO$_2$–MB mixture, the photocatalytic degradation of the MB samples was determined by recording the UV–Vis absorption spectrum in the presence of the CA–TiO$_2$ membrane exposed to different illumination periods of UV light as shown in Fig. 7. Obviously, the photocatalytic degradation activity of CA–TiO$_2$ membrane is more sensitive to the UV illumination period. The maximum value is obtained for the illumination period of

120 min. The percentage photocatalytic activity $A\%$ of the CA–TiO$_2$ membrane can be expressed as

$$A\% = \frac{C_t}{C_o}\%, \tag{4}$$

where C_o is the initial content of the pollutant solution (Blank) and C_t is the final content of the pollutant solution after exposing the mixture of CA–TiO$_2$ membrane and MB to UV illumination for different exposure periods. Figure 8 shows the photocatalytic degradation activity of different membranes in MB dye solution as a function of time. Indeed, repeating the experiment on different samples yields approximately the same influence on the photocatalytic degradation activity of MB dye under UV irradiation. Obviously, a fast photocatalytic degradation activity is observed for CA–TiO$_2$ membrane with the photocatalytic activity of 64.0%. Meanwhile, the lowest activity is observed for CA–CeO$_2$ membrane (7.0%). For better illustration of the degradation rates, the parameter (k) is estimated using the following kinetic equation [42]:

$$\ln\left(\frac{C_t}{C_0}\right) = -kt \tag{5}$$

Figure 9 shows the degradation rate (k) that is calculated from the liner fit of $\ln(C_t/C_0)$ versus the degradation time. For the CA–TiO$_2$, CA–CeO$_2$, and CA–TiO$_2$–CeO$_2$ membranes, the degradation rates are calculated to be 0.0032 min^{-1}, 0.0004 min^{-1}, and
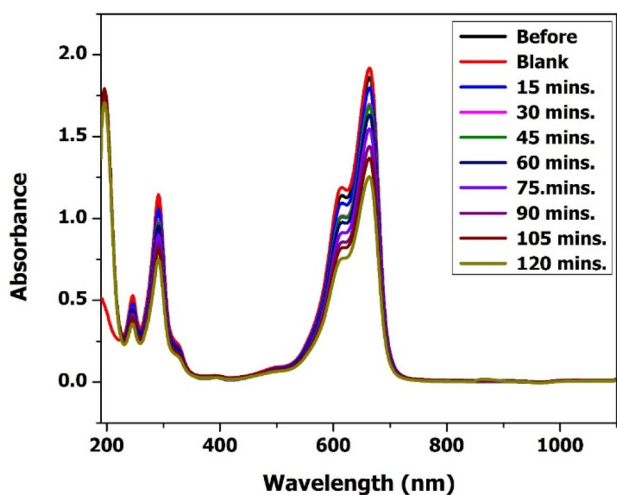
Fig. 7 The MB photocatalytic degradation activity in the presence of the CA–TiO$_2$ membrane exposed to UV illumination every 15-min incremental illumination time
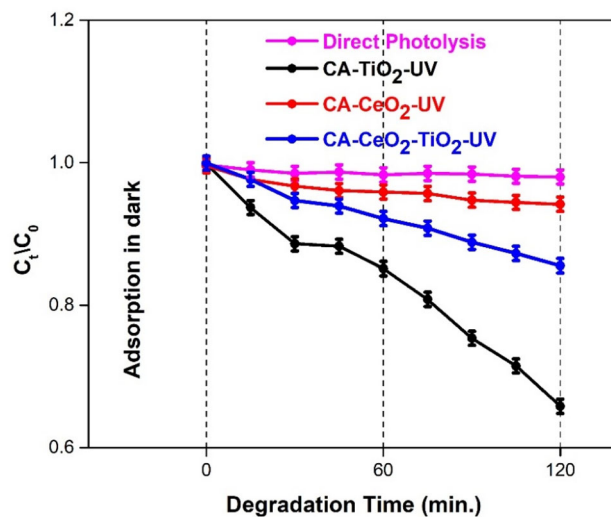
Fig. 8 The photocatalytic degradation activity of MB in the presence of membranes (CA, CA–TiO$_2$, CA–CeO$_2$, and CA–TiO$_2$–CeO$_2$ nanocomposite) exposed to UV irradiation compared to that in dark condition
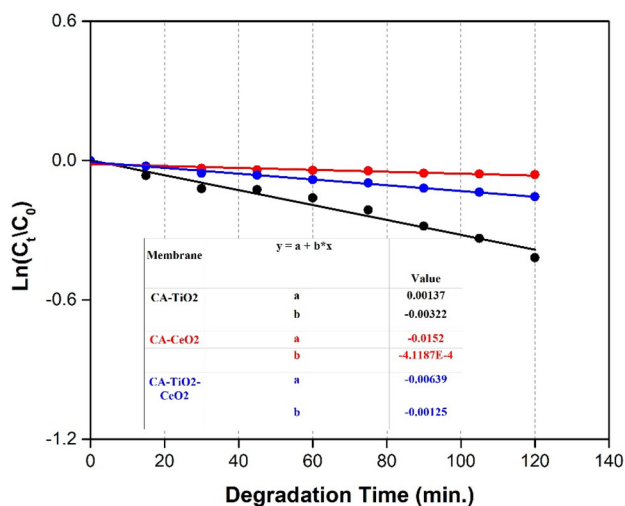
Fig. 9 Plots of $\ln(C/C_0)$ vs. irradiation time for photocatalytic degradation of MB in the presence of CA–NP membranes under UV light and sunlight irradiation

0.0013 min^{-1}, respectively. Obviously, CA–TiO$_2$ membrane exhibits higher photocatalytic degradation activity under UV light that is more than three orders of magnitude than the other two casted CA–NP membranes. The linear fit shown in Fig. 9 reveals that the degradation process of MB adopts first-order kinetics. This could be attributed mainly to the fact that CA–TiO$_2$ membrane exhibits the smallest nanopore size, the most efficient exciton separation, and the highest surface area as compared with CA–CeO$_2$ and CA–TiO$_2$–CeO$_2$-casted membranes. The values of the abovementioned parameters lead to the increase of the number of active sites on the membrane surface and thus leads to higher reactivity [43]. A comparison of the findings of this work on the photocatalytic degradation of MB dye using CA–TiO$_2$ with the results obtained from previous studies is reported in Table 1.

Careful inspection of Table 1 reveals that using a CA–TiO$_2$ membrane for a degradation time of two hours yields a degradation activity of 64% more than TiO$_2$/PVDF membrane that can achieve for a
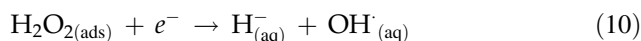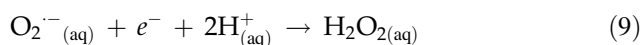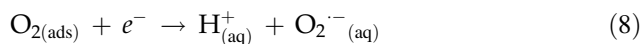
degradation time of five hours. Moreover, its degradation activity is much greater than an Ag/TiO$_2$/PVDF membrane that can produce for approximately the same degradation time.

To elucidate the mechanism of the degradation activity, it is known that anatase TiO2 phase enhances water oxidation to hydroxyl radicals OH·/H$_2$O that is driven by the potential of deep valance shell (band holes h$^+$). However, the reduction of O$_2$ to the superoxide radicals (O$_2$/O$_2$·$^-$) forms hydroxyl radicals which become dominant in the conduction band [46]. Metal oxides such as TiO$_2$ are rich in surface defects especially oxygen vacancy (V$_o$) which often acts as a donor-like state. In the absence of O 2P orbitals, the corresponding electrons transfer into the conduction band generated by Ti 3d orbitals and lead to better photocatalytic activity.
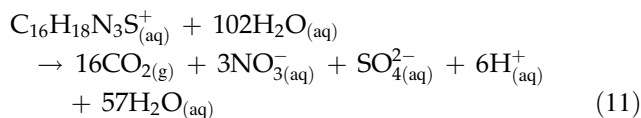
The generation of hydroxyl radicals by oxidation process in valence shells after photoexcitation of TiO$_2$ are described as follows [46]:

$$H_2O_{(ads)} + h^+ \rightarrow H^+_{(aq)} + OH^{\cdot}_{(aq)} \tag{6}$$

$$OH^-_{(aq)} + h^+ \rightarrow H^+_{(aq)} + OH^{\cdot}_{(aq)} \tag{7}$$
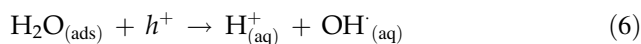
The reduction of oxygen assisted by conduction electrons to form hydroxide radicals can be written as follows [46]:

$$O_{2(ads)} + e^- \rightarrow H^+_{(aq)} + O_2^{\cdot-}{}_{(aq)} \tag{8}$$

$$O_2^{\cdot-}{}_{(aq)} + e^- + 2H^+_{(aq)} \rightarrow H_2O_{2(aq)} \tag{9}$$

$$H_2O_{2(ads)} + e^- \rightarrow H^-_{(aq)} + OH^{\cdot}_{(aq)} \tag{10}$$

The chemical reaction between MB dye and the hydroxyl radicals is described as [46],

$$\begin{aligned} C_{16}H_{18}N_3S^+_{(aq)} + 102H_2O_{(aq)} \\ \rightarrow 16CO_{2(g)} + 3NO^-_{3(aq)} + SO^{2-}_{4(aq)} + 6H^+_{(aq)} \\ + 57H_2O_{(aq)} \end{aligned} \tag{11}$$

The TiO$_2$ NP possess high ratio of oxygen surface defects enabling efficient MB degradation similar to

Table 1 Comparison of photocatalytic degradation activity of MB dye using different membranes

Membrane material	Degradation activity (%)	Irradiation source	Degradation time	MB concentration (mg/L)	References
TiO$_2$/PVDF	60	UV light	5 h	50	[44]
Ag/TiO$_2$/PVDF	51	UV light	100 min	10	[45]
CA–TiO$_2$	64	UV light	2 h	100	This work

CeO$_2$ oxide. Therefore, the aforementioned mechanism is valid to describe the oxidation and reduction on CeO$_2$ NP surface. However, the E_g also plays a crucial role into light absorption and exciton generation, which affect the photocatalytic activity. Moreover, Fig. 10a illustrates the absorbance spectra of all as-prepared CA–NP membranes. Clearly, the three investigated membranes in the visible region exhibit low absorption. Moreover, CA–TiO$_2$ and CA–TiO$_2$–CeO$_2$ nanocomposite membranes exhibit relatively higher absorbance than the CA–CeO$_2$ sample. Figure 10b shows the values of the optical band gap energy of the three CA–NP membranes extracted using Tauc's plot. It gives the relationship between the absorption coefficient (α) and incident photon energy ($h\nu$) in the high absorption region. Tauc plot relation can be written as [47–49]

$$(\alpha h\nu)^{1/n} = A(h\nu - E_g), \quad (12)$$

where A is a constant (band tailing parameter) and n is a power factor that depends on the nature of the material and the type of transition. For direct transitions ($n = 1/2$) and indirect transitions ($n = 2$) [48, 50]. The obtained values of E_g are listed in Table 2. It is worth to mention that the value of E_g strongly depends on parameters, such as, crystal size, strain energy, as well as ions concentration [51, 52].

Figure 11a shows the proposed mechanism of the photocatalytic activity of CA–TiO$_2$ and CeO$_2$ membranes. The locations of the energy of conduction

Table 2 The obtained values of the optical band gap energy (E_g) of the nanoparticles used in this study

NP component	$E_g [eV]$
TiO$_2$	3.26
TiO$_2$–CeO$_2$	3.33
CeO$_2$	3.40

band (E_{CBM}) and valence band (E_{VBM}) versus the normal hydrogen electrode (NHE) of TiO$_2$ and CeO$_2$ are obtained from the previously published works [53, 54]. The photocatalytic mechanism of the CA–TiO$_2$–CeO$_2$ nanocomposite can be illustrated within the framework of Z-scheme heterojunction as shown in Fig. 11b. Currently, the Z-scheme mechanism is intensively employed for discussing that the photocatalytic mechanism is attributed to its merit in explaining the efficient charge separation of photogenerated charge carriers as compared with the conventional type II heterojunction scheme [55, 56]. Obviously, the photoexcited electron in the conduction band of TiO$_2$ is recombined with the photogenerated hole in valence band of CeO$_2$. Consequently, the photoexcited electrons in CeO$_2$ accumulated on conduction band to generate highly reactive species O$_2^{-\cdot}$. Simultaneously, the photocatalytic reaction generate the reactive species OH$^\cdot$ due to the charge accumulation on the valence band of TiO$_2$. Accordingly, the generated reactive species resulted in the degradation of the MB dye.

In this work, the extracted energy gap values are consistent with the photocatalytic activity reported
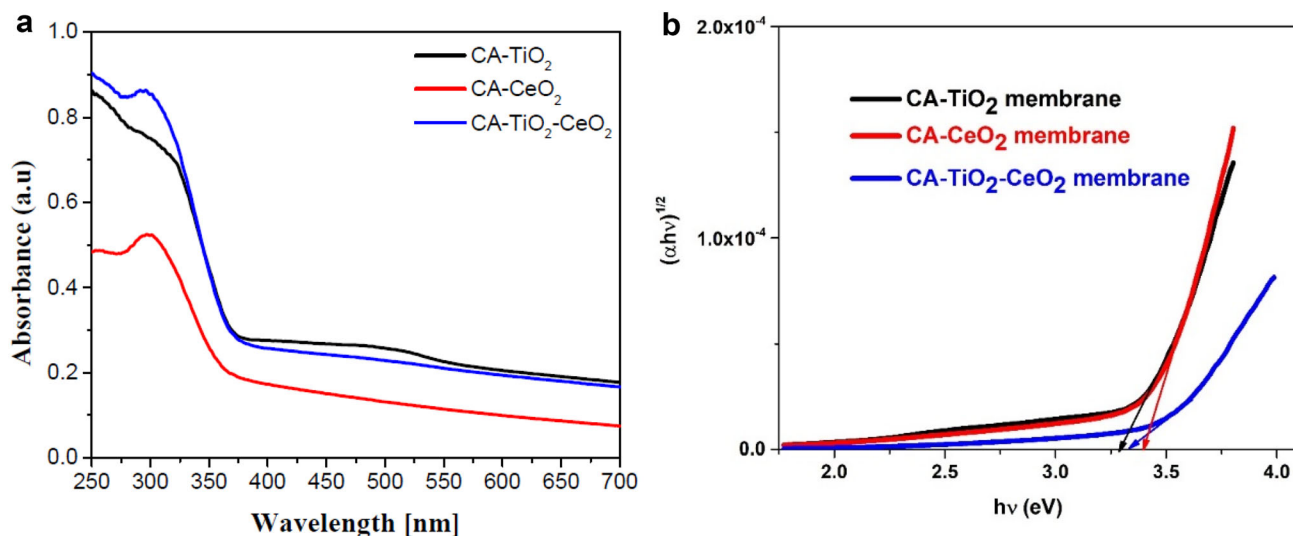

Fig. 10 **a** The absorbance spectra of the three as-prepared CA–NP membranes, and **b** the Tauc plots of the CA–NP membranes utilized to extract the optical band gap energy
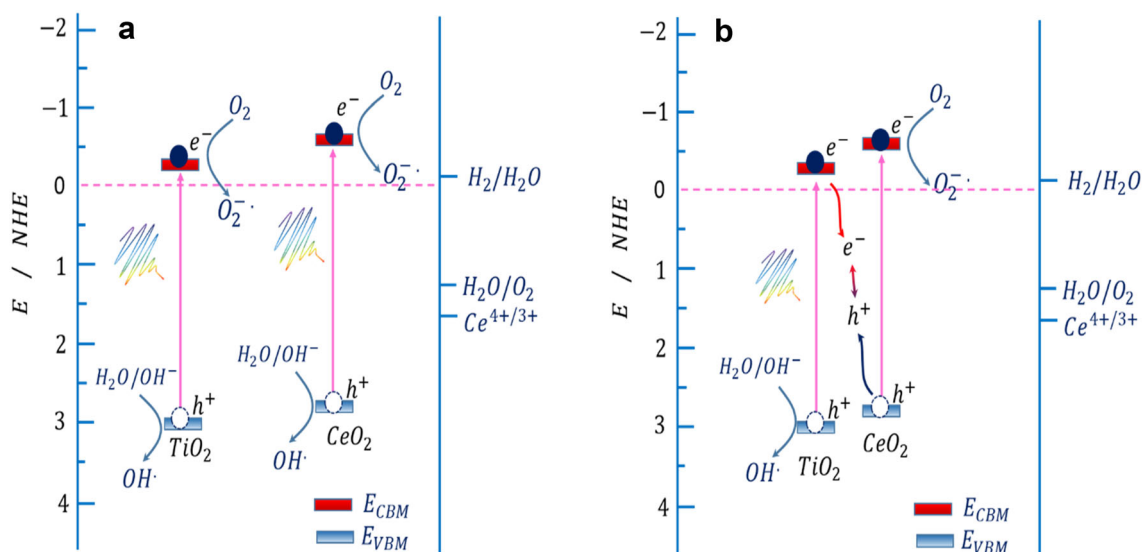
Fig. 11 **a** The mechanism of photocatalytic activity of single junction of CA–TiO$_2$, and **b** the mechanism of photocatalytic activity and charge transfer in a direct Z-scheme heterojunction of CA–TiO$_2$–CeO$_2$ nanocomposite membrane

for different samples. The highest photocatalytic activity is reported for TiO$_2$ that has the lowest E_g. Figure 12 shows the relationship between the photocatalytic degradation activity and the E_g of the three CA–NP membranes. Therefore, the difference in the photocatalytic degradation activity that is observed in Fig. 6 between CA–CeO$_2$ and CA–TiO$_2$ is mainly attributed to the difference in the values of E_g.

The lowest photocatalytic degradation activity of CA–CeO$_2$ can also be interpreted in terms of the high

recombination rate of charge carriers and the low absorbance. In addition, the high porosity and larger surface area of CA–TiO$_2$ membrane enable better photocatalytic degradation activity of MB dye in comparison with those of CA–CeO$_2$–TiO$_2$ and CA–CeO$_2$ membranes. Furthermore, the difference in the E_g leads to enhance charge separation after photoexcitation and subsequently improves the catalytic activity related to the oxidation of O$_2$ and reduction of hydroxyl radicals of the nanocomposite membrane. It is strongly believed that the efficient degradation of CA–TiO$_2$ in comparison with other two investigated membranes is dominated by the value of E_g, as well as the high porosity and the large surface area.

4 Conclusion

In this work, three different CA–NP membranes, namely, CA–TiO$_2$, CA–CeO$_2$, and CA–TiO$_2$–CeO$_2$ nanocomposites, are synthesized systematically using the phase inversion method. All the as-prepared CA–NP membranes exhibited enhanced photocatalytic activity and degradation of MB in aqueous solutions. The results obtained via XRD indicate that the CA–TiO$_2$ membrane showing a main crystalline structure at 25.3° corresponding to Miller indices (101) associated with Anatase crystalline structure and located at the same diffraction angle of CA. The
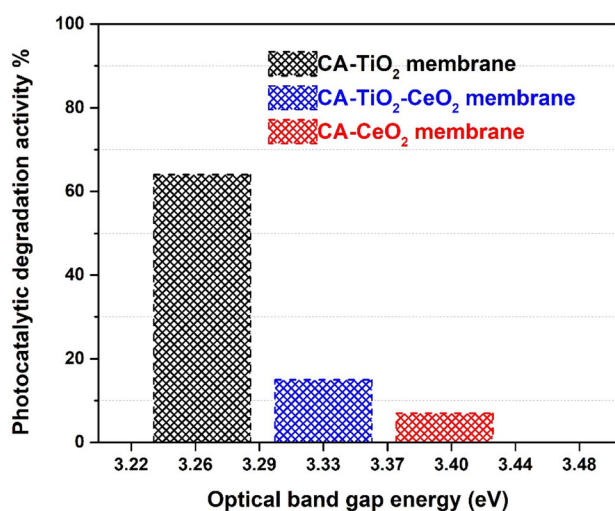

Fig. 12 The photocatalytic degradation activity as a function of the optical E_g of the three CA–NP membranes. Black, blue, and red triangles refer to CA–TiO$_2$, CA–TiO$_2$–CeO$_2$, and CA–CeO$_2$ membranes, respectively

chemical analysis using XRF spectra indicates the presence of 46.6% of TiO_2 NPs and 34.6% of CeO_2 NPs in CA–TiO_2–CeO_2 nanocomposite membranes. The SEM characterization demonstrated that the CA–TiO_2 showed high porosity and large surface area of the membrane compared to CA–CeO_2 and CA–TiO_2–CeO_2 nanocomposite membranes. The photocatalytic degradation of the three different CA–NP membranes impeded in the MB samples revealed that the CA–TiO_2 membrane exhibits the highest degradation activity. This could be attributed mainly to the fact that CA–TiO_2 membrane exhibits the smallest nanopore size, the most efficient exciton separation, and the largest surface area as compared with CA–CeO_2 and CA–TiO_2–CeO_2-casted membranes. Consequently, CA–TiO_2 membrane shows a good cyclic photocatalytic degradation activity on MB as compared with other two casted CA–NP membranes. Furthermore, the degradation activity indicates that as the optical E_g of the NP component of the membrane increases, the degradation activity significantly decreases. The results obtained from this work could revolutionize the perspectives of photocatalytic degradation using the appropriate CA and inorganic metal oxide NP combination.

Author contributions

Conceptualization: BA, AA, BA, SA, and AA; Methodology: BA, AA, BA, SA, and AA; Investigation: BA, AA, BA, SA, and AA; Data curation: BA, AA, BA, SA, AA, and S. Mutlaq; Formal analysis: BA, AA, BA, SA, and AA; Writing—original draft: BA, AA, SA, and AA; Writing—review & editing of the manuscript: BA, AA, BA, and AA; Funding acquisition: AA and BA; Project administration; AA and BA; Resources: AA and BA; Supervision, BA, AA, BA, and AA; Validation: BA, AA, BA, SA, and AA; Visualization: BA, AA, and BA. All authors have read and agreed to the published version of the manuscript.

Data availability

The data presented in this study are available on request from the corresponding author.

Declarations

Conflict of interest The authors declare no conflict of interest (financial or non-financial).

Ethical approval Not applicable.

Informed consent Not applicable.

References

1. N. Yadav et al., Impact of collected sunlight on ZnFe2O4 nanoparticles for photocatalytic application. J. Colloid Interface Sci. **527**, 289–297 (2018)
2. L. Madhura, S. Singh, A review on the advancements of nanomembranes for water treatment. Nanotechnol. Environ. Sci. (2018). https://doi.org/10.1002/9783527808854.ch12
3. M. Nagpal, R. Kakkar, Use of metal oxides for the adsorptive removal of toxic organic pollutants. Sep. Purif. Technol. **211**, 522–539 (2019)
4. Y. Liu et al., Simulated-sunlight-activated photocatalysis of Methylene Blue using cerium-doped SiO_2/TiO_2 nanostructured fibers. J. Environ. Sci. **24**(10), 1867–1875 (2012)
5. Z. Aksu, Application of biosorption for the removal of organic pollutants: a review. Process Biochem. **40**(3–4), 997–1026 (2005)
6. K. Bouziane Errahmani et al., Photocatalytic nanocomposite polymer-TiO_2 membranes for pollutant removal from wastewater. Catalysts **11**(3), 402 (2021)
7. B. Appavu et al., $BiVO_4$/N-rGO nano composites as highly efficient visible active photocatalyst for the degradation of dyes and antibiotics in eco system. Ecotoxicol. Environ. Saf. **151**, 118–126 (2018)
8. C.A. Martínez-Huitle, E. Brillas, Decontamination of wastewaters containing synthetic organic dyes by

electrochemical methods: a general review. Appl. Catal. B **87**(3–4), 105–145 (2009)

9. N.D. Desai et al., Development of dye sensitized TiO_2 thin films for efficient energy harvesting. J. Alloy. Compd. **790**, 1001–1013 (2019)

10. A.M. Al-Diabat et al., A high-sensitivity hydrogen gas sensor based on carbon nanotubes fabricated on SiO_2 substrate. Nanocomposites **7**(1), 172–183 (2021)

11. K. Intarasuwan et al., Photocatalytic dye degradation by ZnO nanoparticles prepared from $X_2C_2O_4$ (X= H, Na and NH4) and the cytotoxicity of the treated dye solutions. Sep. Purif. Technol. **177**, 304–312 (2017)

12. A.-Y. Zhang et al., Degradation of refractory pollutants under solar light irradiation by a robust and self-protected ZnO/CdS/TiO_2 hybrid photocatalyst. Water Res. **92**, 78–86 (2016)

13. A. Fujishima, K. Honda, Electrochemical photolysis of water at a semiconductor electrode. Nature **238**(5358), 37–38 (1972)

14. H. Yan et al., Band structure design of semiconductors for enhanced photocatalytic activity: the case of TiO_2. Prog. Nat. Sci. Mater. Int. **23**(4), 402–407 (2013)

15. K. Nakata, A. Fujishima, TiO_2 photocatalysis: design and applications. J. Photochem. Photobiol. C **13**(3), 169–189 (2012)

16. S. Chen, L.-W. Wang, Thermodynamic oxidation and reduction potentials of photocatalytic semiconductors in aqueous solution. Chem. Mater. **24**(18), 3659–3666 (2012)

17. U. Martinez, B. Hammer, Adsorption properties versus oxidation states of rutile TiO_2 (110). J. Chem. Phys. **134**(19), 194703 (2011)

18. N.A. Deskins, R. Rousseau, M. Dupuis, Defining the role of excess electrons in the surface chemistry of TiO_2. J. Phys. Chem. C **114**(13), 5891–5897 (2010)

19. S. Tanigawa, T. Takashima, H. Irie, Enhanced visible-light-sensitive two-step overall water-splitting based on band structure controls of titanium dioxide and strontium titanate. J. Mater. Sci. Chem. Eng. **5**(01), 129 (2017)

20. T. Mano et al., Water treatment efficacy of various metal oxide semiconductors for photocatalytic ozonation under UV and visible light irradiation. Chem. Eng. J. **264**, 221–229 (2015)

21. M. Pawar, S. Topcu Sendoğdular, P. Gouma, A brief overview of TiO_2 photocatalyst for organic dye remediation: case study of reaction mechanisms involved in Ce–TiO_2 photocatalysts system. J. Nanomater. **2018**, 1–13 (2018)

22. F.E. Ahmed, B.S. Lalia, R. Hashaikeh, A review on electrospinning for membrane fabrication: challenges and applications. Desalination **356**, 15–30 (2015)

23. N.H. Alias et al., Photocatalytic materials-based membranes for efficient water treatment, in *Handbook of Smart Photocatalytic Materials*. (Elsevier, 2020), pp. 209–230

24. H. Matsuyama et al., Porous cellulose acetate membrane prepared by thermally induced phase separation. J. Appl. Polym. Sci. **89**(14), 3951–3955 (2003)

25. S.H. Paiman et al., Functionalization effect of Fe-type MOF for methylene blue adsorption. J. Saudi Chem. Soc. **24**(11), 896–905 (2020)

26. S. Lvov et al., Nafion®/TiO_2 composite membranes for PEM fuel cells operating at elevated temperature and reduced relative humidity. ECS Trans. **3**(1), 73 (2006)

27. V. Baglio et al., Influence of TiO_2 nanometric filler on the behaviour of a composite membrane for applications in direct methanol fuel cells. J. New Mater. Electrochem. Syst. **7**, 275–280 (2004)

28. G. Arthanareeswaran et al., Synthesis, characterization and thermal studies on cellulose acetate membranes with additive. Eur. Polym. J. **40**(9), 2153–2159 (2004)

29. X. Wang et al., Preparation, characterisation, and desalination performance study of cellulose acetate membranes with MIL-53 (Fe) additive. J. Membr. Sci. **590**, 117057 (2019)

30. S.D. Delekar et al., Structural and optical properties of nanocrystalline TiO_2 with multiwalled carbon nanotubes and its photovoltaic studies using Ru (II) sensitizers. ACS Omega **3**(3), 2743–2756 (2018)

31. S. Delekar et al., Molecular self-assembled designing and characterization of TiO_2 NPs-CdS QDs-dye composite for photoanode materials. Mater. Charact. **139**, 337–346 (2018)

32. S. Mourdikoudis, R.M. Pallares, N.T. Thanh, Characterization techniques for nanoparticles: comparison and complementarity upon studying nanoparticle properties. Nanoscale **10**(27), 12871–12934 (2018)

33. D.A. Hanaor, C.C. Sorrell, Review of the anatase to rutile phase transformation. J. Mater. Sci. **46**(4), 855–874 (2011)

34. I.-C. Kim, K.-H. Lee, Effect of poly (ethylene glycol) 200 on the formation of a polyetherimide asymmetric membrane and its performance in aqueous solvent mixture permeation. J. Membr. Sci. **230**(1–2), 183–188 (2004)

35. P. Thistlethwaite, M. Hook, Diffuse reflectance Fourier transform infrared study of the adsorption of oleate/oleic acid onto titania. Langmuir **16**(11), 4993–4998 (2000)

36. K. Zhang, K.C. Kemp, V. Chandra, Homogeneous anchoring of TiO2 nanoparticles on graphene sheets for waste water treatment. Mater. Lett. **81**, 127–130 (2012)

37. Y. Chen et al., Effective photocatalytic degradation and physical adsorption of methylene blue using cellulose/GO/TiO_2 hydrogels. RSC Adv. **10**(40), 23936–23943 (2020)

38. Y. Alqaheem, A.A. Alomair, Microscopy and spectroscopy techniques for characterization of polymeric membranes. Membranes **10**(2), 33 (2020)

39. M.E. Culica et al., Cellulose acetate incorporating organically functionalized CeO_2 NPs: efficient materials for UV filtering applications. Materials **13**(13), 2955 (2020)

40. X. Jin et al., Flexible TiO_2/cellulose acetate hybrid film as a recyclable photocatalyst. RSC Adv. **4**(25), 12640–12648 (2014)

41. S. Chougule et al., Low density polyethylene films incorporated with Biosynthesised silver nanoparticles using Moringa oleifera plant extract for antimicrobial, food packaging, and photocatalytic degradation applications. J. Plant Biochem. Biotechnol. **30**(1), 208–214 (2021)

42. M.A. Abu-Dalo, S.A. Al-Rosan, B.A. Albiss, Photocatalytic degradation of methylene blue using polymeric membranes based on cellulose acetate impregnated with ZnO nanostructures. Polymers **13**(19), 3451 (2021)

43. A.O. Ibhadon, P. Fitzpatrick, Heterogeneous photocatalysis: recent advances and applications. Catalysts **3**(1), 189–218 (2013)

44. T. Li et al., A membrane modified with nitrogen-doped TiO2/graphene oxide for improved photocatalytic performance. Appl. Sci. **9**(5), 855 (2019)

45. J.-H. Li et al., Influence of Ag/TiO_2 nanoparticle on the surface hydrophilicity and visible-light response activity of polyvinylidene fluoride membrane. Appl. Surf. Sci. **324**, 82–89 (2015)

46. J. Harris et al., Hierarchical TiO_2 nanoflower photocatalysts with remarkable activity for aqueous methylene blue photo-oxidation. ACS Omega **5**(30), 18919–18934 (2020)

47. M. Tommalieh et al., Characterization and electrical enhancement of PVP/PVA matrix doped by gold nanoparticles prepared by laser ablation. Radiat. Phys. Chem. **179**, 109195 (2021)

48. P. Dhatarwal, R. Sengwa, Nanofiller controllable optical parameters and improved thermal properties of (PVP/PEO)/Al_2O_3 and (PVP/PEO)/SiO_2 nanocomposites. Optik **233**, 166594 (2021)

49. A.M. Al-Diabat et al., Influence of the spray distance to substrate on optical properties of chemically sprayed ZnS thin films. J. Mater. Sci. Mater. Electron. **28**(1), 371–375 (2017)

50. A. Alsaad et al., Synthesis and characterization of as-grown doped polymerized (PMMA-PVA)/ZnO NPs hybrid thin films. Polym. Bull. **79**(4), 2019–2040 (2022)

51. K. Joshi et al., Band gap widening and narrowing in Cu-doped ZnO thin films. J. Alloy. Compd. **680**, 252–258 (2016)

52. S. Aksoy et al., Effect of Sn dopants on the optical and electrical properties of ZnO films. Opt. Appl. **40**(1), 7–14 (2010)

53. M.D. Hernández-Alonso et al., Development of alternative photocatalysts to TiO_2: challenges and opportunities. Energy Environ. Sci. **2**(12), 1231–1257 (2009)

54. R. Ma et al., Transformation of CeO_2 into a mixed phase CeO_2/Ce_2O_3 nanohybrid by liquid phase pulsed laser ablation for enhanced photocatalytic activity through Z-scheme pattern. Ceram. Int. **42**(16), 18495–18502 (2016)

55. K. Qi et al., A review on TiO_2-based Z-scheme photocatalysts. Chin. J. Catal. **38**(12), 1936–1955 (2017)

56. J. Wang et al., ZnO nanoparticles implanted in TiO_2 macrochannels as an effective direct Z-scheme heterojunction photocatalyst for degradation of RhB. Appl. Surf. Sci. **456**, 666–675 (2018)